Because  $\Delta n(z)$  is periodic, it can be decomposed into the Fourier series

$$\Delta n(z) = \sum_{p = -\infty}^{\infty} \Delta n_p \ e^{ip\frac{2\pi}{\Lambda}z}.$$
 (8.5.21)

Therefore,

$$\Delta \varepsilon_{p} = 2n_{0} \, \Delta n_{p} \quad \text{for } |x| \leq d/2, \quad \text{and} \quad \Delta \varepsilon_{p} = 0 \quad \text{for } |x| > d/2$$

$$K_{ab} = \frac{\omega \varepsilon_{0}}{4} \int_{|x| \leq \frac{d}{2}} \Delta \varepsilon_{p}(x) \left| E_{y}^{(0)}(x) \right|^{2} dx$$

$$= \frac{\omega \varepsilon_{0}}{4} (2n_{0} \Delta n_{+1}) \frac{2\omega \mu}{\beta} \Gamma$$

$$\simeq \Gamma k_{0} \Delta n_{+1} \qquad (8.5.22)$$

where  $k_0 = \omega \sqrt{\mu_0 \varepsilon_0}$ , and  $\beta_0 = k_0 n_0$  have been used, and  $\Gamma$  is exactly the optical confinement factor because we assume the index grating is dependent on z inside the guide. Similarly,

$$K_{ba} \simeq -\Gamma k_0 \Delta n_{-1} \tag{8.5.23}$$

and we have kept p = +1 or -1 for the first-order grating.

For an index phase grating with a magnitude  $\Delta n$  and phase  $\varphi$ ,

$$\Delta n(z) = \Delta n \cos\left(\frac{2\pi}{\Lambda}z + \varphi\right)$$

$$= \Delta n_{+1} e^{\frac{i2\pi}{\Lambda}z} + \Delta n_{-1} e^{-\frac{i2\pi}{\Lambda}z}$$

$$\Delta n_{+1} = \frac{\Delta n}{2} e^{i\varphi}, \qquad \Delta n_{-1} = \frac{\Delta n}{2} e^{-i\varphi}.$$
(8.5.24)

The coupling coefficients are

$$K_{ab} = \Gamma k_0 \frac{\Delta n}{2} e^{i\varphi} \tag{8.5.25a}$$

$$K_{ba} = -\Gamma k_0 \frac{\Delta n}{2} e^{-i\varphi} = -K_{ab}^* \tag{8.5.25a}$$

In other words, the coupling coefficients can be put in very simple forms and they satisfy the relation  $K_{ba}=-K_{ab}^*$  because the index grating is lossless.

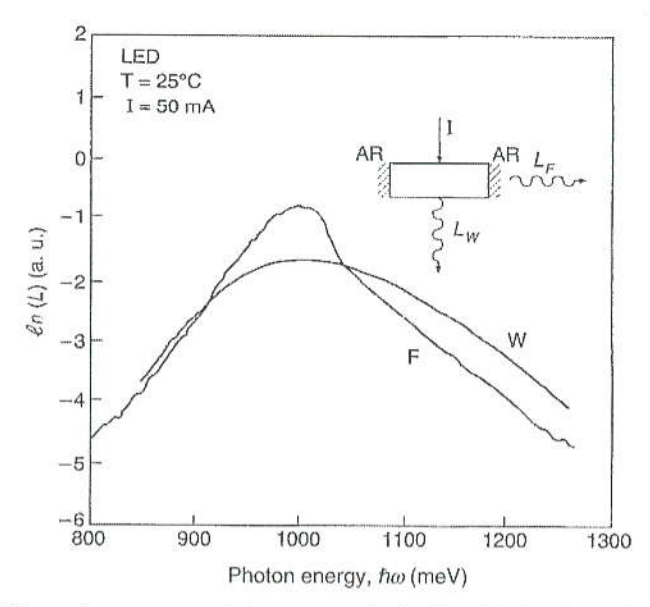


Figure 10.8 Measured spontaneous emission spectrum obtained by collecting photons through a window (W) in the substrate  $L_W$  and the amplified spontaneous emission spectrum obtained by collecting photons from the facet (F)  $L_F$  of an LED. (Reprinted with permission from [42] © 1993 American Institute of Physics.)

where  $G_n(\hbar\omega) = \Gamma g - \alpha_i$  is the net modal gain (including all the losses due to absorptions and scatterings in the device). Note that at the transparency wavelength,  $G_n(\hbar\omega) = 0$  and  $L_F(\hbar\omega) = L_W(\hbar\omega)$  when no amplification by the gain action exists. With enough carrier injection such that  $G_n > 0$ , we see that the photon density in the spectral region where  $g(\hbar\omega)$  is positive will experience amplification whereas that outside the positive gain region will experience absorption. Because the gain spectrum is narrower than that of the spontaneous emission spectrum [46], the facet light will be narrower than that of the window light. These results [42] are shown in Fig. 10.8. As a matter of fact, a comparison of these two spectra has been used to extract the gain spectrum of a laser diode structure. By measuring the two spectra  $L_F(\hbar\omega)$  and  $L_W(\hbar\omega)$  at the same current injection level, we can obtain the gain spectrum. Furthermore, if we take the logarithmic function of the ratio of the two spectra,  $\ln [L_F(\hbar\omega)/L_W(\hbar\omega)]$ , it will be close to that of the gain spectrum because it is proportional to  $\ln [(e^{G_nL}-1)/G_n] \sim (\Gamma g -\alpha_i)L$  if the overall gain  $(G_n L \gg 1)$  is large enough [43]. By fitting the gain spectrum with a theoretical gain model, we can extract the carrier density n at a given injection current I [43]. The carrier density versus the injection current I is a monotonically increasing function of I, as shown in Fig. 10.9a at 25°C and Fig. 10.9b at 55°C. For laser diodes, the carrier density is pinned at the threshold value when the injection current is increased beyond threshold.

delete subscript n current density is called the transparent current density. Further increase of the current increases gain until it reaches the threshold condition, at which the gain is equal to the background absorption plus the mirror transmission loss (or laser output) of the cavity.

Consider an optical field  $E_{\rm sp}(\lambda)$  due to the spontaneous emission of photons by electron-hole radiative recombinations in a Fabry-Perot cavity. When the optical field propagates toward the minor facets with optical field reflection coefficients  $r_1$  and  $r_2$  on each facet, we can write down the multiple reflections of the optical field as

$$E_{ASE}(\lambda) = E_{sp}(\lambda) \left[ 1 + r_1 r_2 e^{i2kL} + \left( r_1 r_2 e^{i2kL} \right)^2 + \cdots \right]$$

$$= \frac{E_{sp}(\lambda)}{1 - r_1 r_2 e^{i2kL}}.$$
(10.1.29)

The complex propagation constant has a real and imaginary part

$$k = k' - i\frac{G_n}{2} = \frac{2\pi}{\lambda}n_e - i\frac{G_n}{2}$$
 (10.1.30a)

$$G_n = \Gamma g - \alpha_i = \text{The } net \text{ modal gain.}$$
 (10.1.30b)

The measured ASE power spectrum is proportional to  $|E_{ASE}(\lambda)|^2$ 

$$I(\lambda) = |E_{ASE}(\lambda)|^2 = \frac{|E_{sp}(\lambda)|^2}{|1 - r_1 r_2 e^{i2kL}|^2} = \frac{|E_{sp}(\lambda)|^2}{(1 - A)^2 + 4A\sin^2(k'L)}$$
(10.1.31)

where the amplitude A is

$$A = \sqrt{R_1 R_2} e^{G_n L}, \quad R_1 = |r_1|^2, \quad R_2 = |r_2|^2.$$
 (10.1.32)

The ASE spectrum has maxima at

$$k'L = m\pi, \quad I_{\text{max}} = \frac{|E_{\text{sp}}(\lambda_{\text{max}})|^2}{(1 - A)^2}$$
 (10.1.33a)

and minima at

$$k'L = \left(m + \frac{1}{2}\right)\pi, \quad I_{\min} = \frac{|E_{\rm sp}(\lambda_{\rm min})|^2}{(1+A)^2}.$$
 (10.1.33b)

Imin

If we take the ratio between two nearby peak and valley of the ASE spectrum,

$$\frac{I_{\text{max}}}{I_{\text{min}}} = \frac{(1+A)^2}{(1-A)^2} \tag{10.1.34a}$$

Because  $k_z/\omega\mu$  is a constant for a given mode, we can simply use

$$\Gamma = \frac{\int \int_{\text{active}} |E_y(x, y)|^2 dx dy}{\int_{-\infty}^{\infty} \int_{-\infty}^{\infty} |E_y(x, y)|^2 dx dy} \simeq \Gamma_x \Gamma_y$$
 (10.2.11)

which is approximated by the product of the two optical confinement factors along the *x* direction (with a slab geometry in the effective index method) and along the *y* direction when the field is approximately given by

$$E_{\mathbf{y}} \simeq F(\mathbf{x}) G(\mathbf{y}). \tag{10.2.12}$$

It is a good approximation for a strongly index-guided structure, and  $F(x, y) \simeq F(x)$  if the geometry along the y direction is uniform such that the first part of the wave function F(x, y) in the effective index method described in Section 7.5 can be assumed to be independent of y. Index-guided semiconductor lasers have been shown to exhibit excellent performance including the fundamental mode operation, low threshold, high quantum efficiency, and low temperature sensitivity [33].

#### 10.3 QUANTUM-WELL LASERS

Quantum-well (QW) structures [12–16, 61], as shown in Fig. 10.19, have been used as the active layer of semiconductor laser diodes with reduced threshold current densities compared with those for conventional double-heterostructure (DH) semiconductor diode lasers. Research on quantum-well physics and semiconductor lasers has been of great interest recently. For a brief history, see Ref. 3. Various designs such as single quantum well (SQW), multiple quantum well (MQW), and graded-index separate-confinement heterostructures (GRINSCH) have been used for semiconductor lasers [21]. As we have seen in Chapter 9, quantum-well structures show quantized subbands and step-like densities of states. The density of states for a quasi-two-dimensional structure has been used to reduce threshold current density and improve temperature stability. Energy quantization provides another degree of freedom to tune the lasing wavelength by varying the well width and the barrier height. Scaling laws for quantum-well lasers and quantum-wire lasers show significant reduction of threshold current in reduced dimensions [24].

#### 10.3.1 A Simplified Gain Model

The simplest model we will consider is the gain spectrum based on (9.4.18) for a finite temperature, assuming a zero scattering linewidth [62, 63]

$$g(\hbar\omega) = \sum_{n,m} g_{\text{max}} [f_c^n (E_t = \hbar\omega - E_{hm}^{en}) - f_v^m (E_t = \hbar\omega - E_{hm}^{en})] H(\hbar\omega - E_{hm}^{en})$$
(10.3.1a)

where

$$g_{\text{max}} = C_0 |\hat{e} \cdot \mathbf{M}|^2 |I_{hm}^{en}|^2 \rho_{\text{r}}^{\text{2D}} \simeq C_0 |\hat{e} \cdot \mathbf{M}|^2 \rho_{\text{r}}^{\text{2D}} \delta_{nm}$$
 (10.3.1b)

$$C_0 = \frac{\pi e^2}{n_{\rm r} c \, \varepsilon_0 m_0^2 \omega} \qquad \rho_{\rm r}^{\rm 2D} = \frac{m_{\rm r}^*}{\pi \hbar^2 L_z}$$
 (10.3.1c)

13

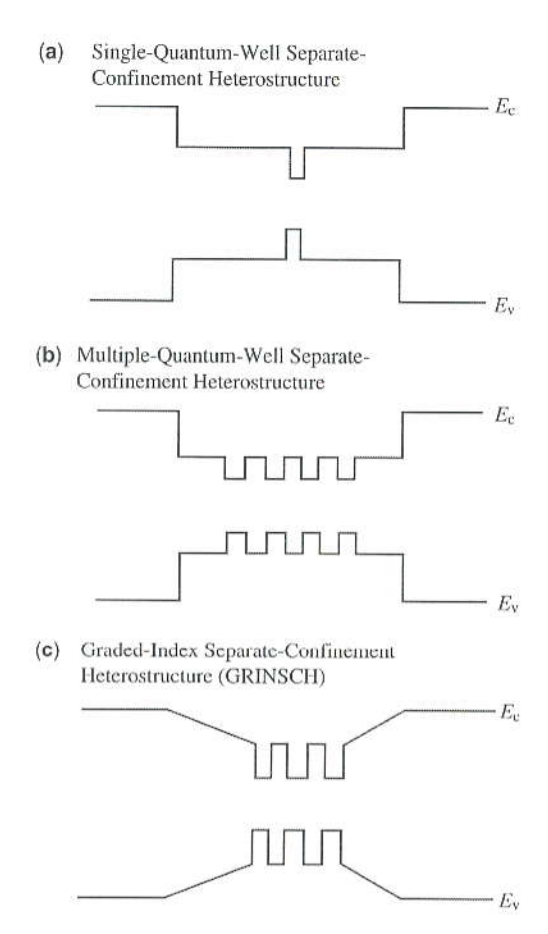


Figure 10.19 Band-gap profiles for (a) single-quantum-well, (b) multiple-quantum-well, and (c) graded-index separate-confinement heterostructure (GRINSCH) semiconductor lasers.

is the reduced joint density of states. The overlap integral between the nth conduction subband and the mth hole subband is usually very close to unity for n=m, and it vanishes if  $n \neq m$  because of the even-odd parity consideration. The polarization-dependent momentum matrix element is listed in Table 9.1 for conduction to heavy-hole and light-hole band transitions. The occupation factors for the electrons in the nth conduction subband and the electrons in the mth hole subband are

$$f_{c}^{n}(E_{t} = \hbar\omega - E_{hm}^{en}) = \frac{1}{1 + e^{\left[E_{en} + (m_{r}^{*}/m_{c}^{*})(\hbar\omega - E_{hm}^{en}) - F_{c}\right]/k_{B}T}}$$
(10.3.2a)

$$f_{v}^{m}\left(E_{l} = \hbar\omega - E_{hm}^{en}\right) = \frac{1}{1 + e^{\left[E_{hm} - (m_{v}^{*}/m_{h}^{*})(\hbar\omega - E_{hm}^{en}) - F_{v}\right]/k_{B}T}}.$$
 (10.3.2b)

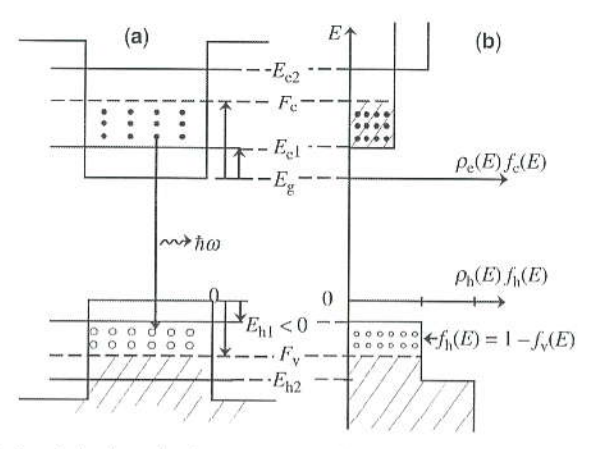


Figure 10.20 (a) Population inversion in a quantum-well structure, where  $E_g + F_c - F_v > \hbar\omega > E_{e1} - E_{h1} + E_g$ . (b) The product of the conduction band density of states  $\rho_c(E)$  and the Fermi-Dirac occupation probability  $f_c(E)$  for the calculation of the electron density n is plotted versus the energy E in the vertical scale. Similarly,  $\rho_h(E) f_h(E) = \rho_h(E) [1 - f_v(E)]$  is plotted versus E for the energy (E < 0) in the valence band. Assume that the temperature T is 0K.

Gain occurs when  $f_{\rm c}^n > f_{\rm v}^m$ , that is, the population inversion is achieved, Fig. 10.20. It also leads to  $E_{\rm g} + F_{\rm c} - F_{\rm v} > \hbar \omega$ , where  $F_{\rm c}$  and  $F_{\rm v}$  are the quasi-Fermi levels for electrons and holes, measured from the conduction and valence band edges, respectively. Only those electrons and holes satisfying the k-selection rule contribute significantly to the gain process.

### 10.3.2 Determination of Electron and Hole quasi-Fermi Levels

The quasi-Fermi levels  $F_c$  and  $F_v$  are determined by the carrier concentrations n and p, which satisfy the charge neutrality condition

$$n + N_{A}^{-} = p + N_{D}^{+}$$

$$n = \int_{0}^{\infty} dE \, \rho_{e}(E) f_{c}(E), \quad p = \int_{-\infty}^{\infty} dE \, \rho_{h}(E) [1 - f_{v}(E)]$$

$$\rho_{e}(E) = \frac{m_{e}^{*}}{\pi h^{2} L_{z}} \sum_{n=1}^{\infty} H(E - E_{en})$$

$$\rho_{h}(E) = \frac{m_{h}^{*}}{\pi h^{2} L_{z}} \sum_{m=1}^{\infty} H(E_{hm} - E)$$

$$(10.3.4)$$



where H(x) is the Heaviside step function, H(x) = 1 if x > 0, and H(x) = 0 if x < 0. In Fig. 10.21a and Fig. 10.21b, we plot the products  $p_c(E) f_c(E)$  and  $p_h(E) [1 - f_v(E)]$  versus the energy E for T = 0K and 300K, respectively. The areas below these functions give the carrier concentrations n and p.

Figure 10.43 shows [133] an example of self-organized InAs quantum dots inserted in InGaAs quantum well grown on a GaAs substrate by molecular-beam epitaxy. Room temperature photoluminescence spectrum shows that QD emission wavelength is controllable from 1.1 to 1.3 µm by varying the composition of  $In_xGa_{1-x}As$  quantum-well matrix from x = 0 (1.1  $\mu$ m for GaAs matrix) to x = 0.3(1.3 μm). Figure 10.44a [133] shows the plan-view bright-field TEM image along [100] direction and Fig. 11.44b the cross-section image under dark-field (200) condition for the InAs QD array in a 10-nm In<sub>0.12</sub>Ga<sub>0.88</sub>As quantum well. InAs-rich clusters in the region of smaller InAs content are seen in both observation views. The surface density of the islands is estimated as  $(3-4)\times10^{10}$  cm<sup>-2</sup>. The dots have a typical lateral size of about 20 nm and a height of 5-6 nm. These sizes are larger than those of the InAs islands formed in a GaAs matrix. Because both the QD and QW materials are lattice mismatched to the GaAs substrate, there is a risk of plastic strain relaxation. Nevertheless, no misfit dislocations are revealed by TEM due to the choice of the QW width and the InAs model fraction in the QW [133]. The sample with the QD structure embedded in a vertical optical microcavity shows a Photoluminescence (PL) emission of 1.33 µm [133].



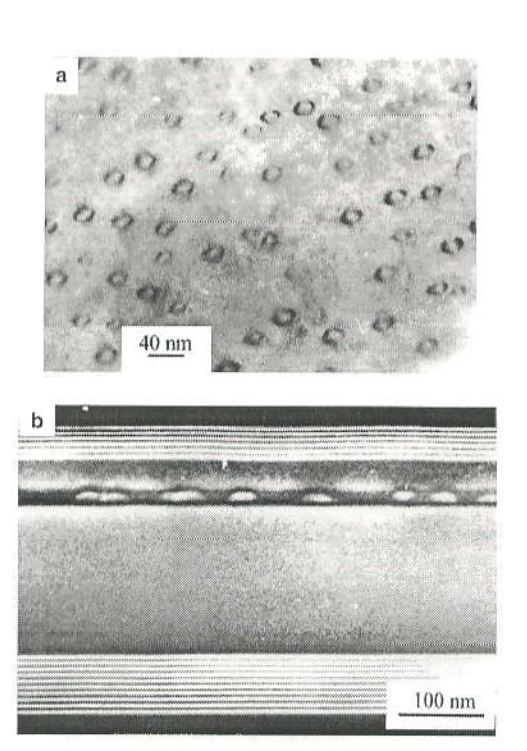


Figure 10.44 (a) Plan-view of the bright-field TEM image along the [100] zone, and (b) the image of the cross section under dark-field (200) condition for the structure containing InAs QD array in a 10-nm In<sub>0.12</sub>Ga<sub>0.88</sub>As QW. (Reprinted with permission from [133] © 1999 American Institute of Physics.)

### 10.5.2 Spontaneous Emission, Gain, and Lasing Spectrum

In Chapter 9, we discussed the absorption and gain of quantum-dot lasers [140–146]. The filling of states of quantum dots is complicated by the inhomogeneous size distribution and the density of dots or the distance between nearby dots [141]. When the inhomogeneous broadening is reduced, clear observation of ground-state and excited-state emission peaks or absorption peaks are observable [141–146]. For example, Fig. 10.45a [141] shows the net model absorption of a quantum-dot sample (dots in a well, or DWELL [139]) showing clear absorption peaks at the ground state and excited state when there is no current injection. In the presence of increasing current, population inversion occurs and a clear gain peak occurs at the ground state or the excited state at a higher current of 200 mA. Analysis of the gain spectrum seems to indicate two quasi-Fermi levels for the ground and excited state. The competition of homogenous broadening and inhomogeneous broadening also leads to

- modal

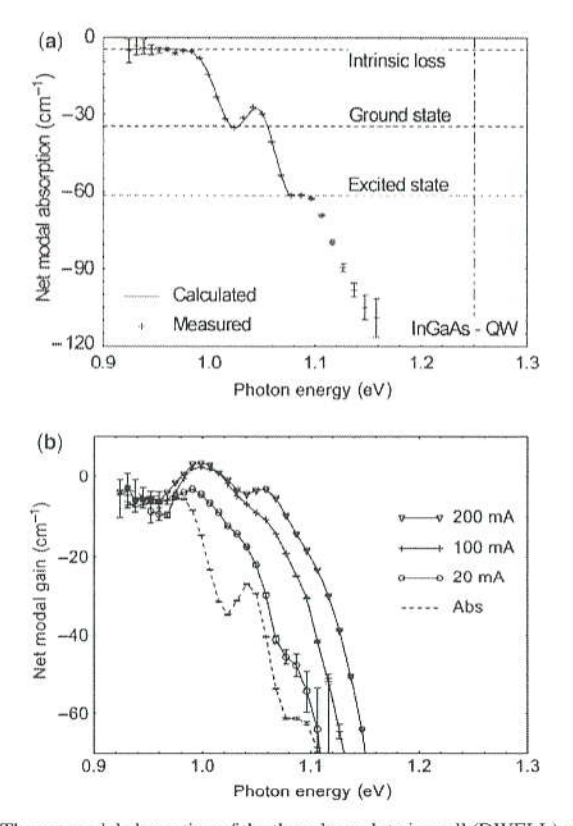


Figure 10.45 (a) The net modal absorption of the three-layer dots-in-well (DWELL) waveguide structure for TE-polarized light. The vertical line indicates the transition energy of the well. The horizontal dashed lines indicate the waveguide loss and the peak absorptions due to the ground and excited states. The solid line is the fitting of the calculated absorption spectrum to the experimental data. (b) The net modal TE gain spectra for pulsed currents per segment from 20 to 200 mA. (Reprinted with permission from [141] © 2004 IEEE.)

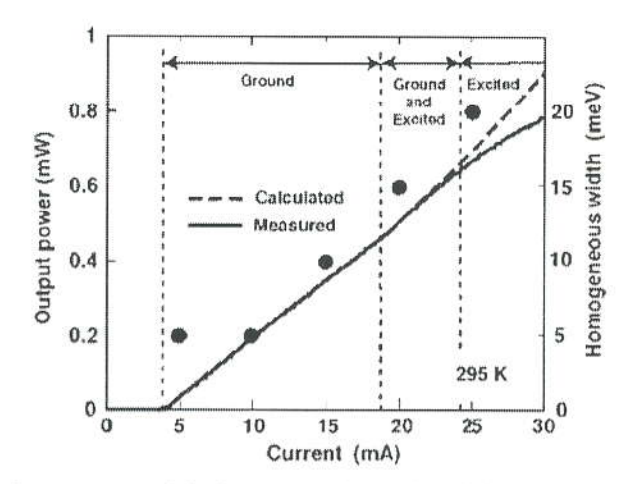


Figure 10.47 Output power and the homogeneous broadening of the ground-state transition (solid circles) versus the injection current at 295K. The solid curve is the measurement, and the dashed curve is the calculation. The range of current for only the ground-state lasing, both the ground-state and excited-state lasings, and only the excited-state lasing is shown, with the perpendicular dashed lines as boundaries. (Reprinted with permission from [142] © 2005 American Institute of Physics.)

only the excited state are marked. The homogenous linewidth, which is used to model the lasing spectrum, is also shown as the right vertical axis.

### 10.5.3 High-Speed Modulation: p-Doping and Tunneling Injection

p-Type Doping [147-162] A few major improvements in quantum-dot lasers result from the p-type doping, tunneling injection, and submonolayer growth (for a recent review, see [137]. p-type doping was suggested as early as 1988 [127] to improve the gain property of quantum-dot lasers. A simple way to understand the advantage of p-type doing is that the heavy-hole subband energy levels are close to each other due to their heavier effective mass than that of the electrons in the conduction band. Therefore, the holes spread out thermally into various subbands instead of filling the ground state completely first, whereas electrons tend to occupy the ground state better because the excited state of the conduction subband (C2) is further away from the ground state (C1). It implies that the number of interband transitions such as C1-HH1 is reduced because not all holes occupy the ground state (HH1) for an undoped quantum dot sample. The holes that spread out to HH2 subband do not recombine effectively with those electrons of the C1 subband. Although this is an oversimplified picture, theoretical models and experimental data seem to confirm several advantages of p-type doping. Experimental results have indeed shown that the p-doped 1.3-\mu QD lasers have substantially improved performance for short cavity lengths, indicating an increase in the ground state gain and exhibit excellent temperature sensitivity [147-149]. Further experimental data [149] on spontaneous and laser emission of p-doped and undoped QD heterostructures indeed show that the ground-state spontaneous emission of the carbon-doped

- insensitivity

·t

### 12.2 HIGH-SPEED MODULATION RESPONSE WITH NONLINEAR GAIN SATURATION

### 12.2.1 Nonlinear Gain Saturation

The nonlinear gain model g(n, S) at high photon density S can be taken from [12, 13]

$$g(n, S) = \frac{g(n_0) + g'(n(t) - n_0)}{1 + \varepsilon S(t)}$$
(12.2.1)

where  $g_0 = g(n_0)$  and  $g' = [\partial g/\partial n]_{n=n_0}$  is the differential gain at  $n_0$ . The factor  $1 + \varepsilon S$  accounts for nonlinear gain saturation, which is important when the photon density is large. The factor  $\varepsilon$  is called the gain suppression coefficient.

**dc Solution** The steady-state solution at  $I = I_0$  is obtained from d/dt = 0 in the rate equations

$$\eta_{\rm i} \frac{J_0}{qd} = \frac{n_0}{\tau} + \frac{{\rm v_g} g_0 S_0}{1 + \varepsilon S_0}$$
(12.2.2)

$$\Gamma \frac{v_{\rm g} g_0 S_0}{1 + \varepsilon S_0} = \frac{S_0}{\tau_{\rm p}} - \beta R_{\rm sp}(n_0). \tag{12.2.3}$$

If  $\varepsilon \neq 0$ , the general solution for  $S_0$  can be found analytically from (12.2.3) (see Problem 12.5). Then  $n_0$  is obtained from (12.2.2).

**Small Signal ac Analysis** Using the linearized expression by substituting (12.1.10) into (12.2.1), we obtain

$$g(n, S) = \frac{g(n_0)}{1 + \varepsilon S_0} + \frac{g'}{1 + \varepsilon S_0} \Delta n(t) - \frac{g_0}{(1 + \varepsilon S_0)^2} \varepsilon s(t).$$
 (12.2.4)

The small signal ac responses  $\Delta n(t)$  and s(t) satisfy the following equations

$$\frac{d}{dt} \begin{bmatrix} \Delta n(t) \\ s(t) \end{bmatrix} + \begin{bmatrix} A & D \\ -C & B \end{bmatrix} \begin{bmatrix} \Delta n(t) \\ s(t) \end{bmatrix} = \begin{bmatrix} \eta_i j(\boldsymbol{\phi})/qd \\ 0 \end{bmatrix}$$
(12.2.5)

where A, B, C, and D are defined as

$$A = \frac{1}{\tau} + \frac{v_g g' S_0}{1 + \varepsilon S_0} \qquad B = \frac{1}{\tau_p} - \frac{\Gamma v_g g_0}{(1 + \varepsilon S_0)^2}$$

$$C = \frac{\Gamma v_g g' S_0}{1 + \varepsilon S_0} \qquad D = \frac{v_g g_0}{(1 + \varepsilon S_0)^2}.$$
(12.2.6)

small-signal frequency response of the test laser for optical modulation from the pump laser and use the same rate equations with a different source term to derive the electrical modulation response of the test laser.

Electrical Injection For electrical microwave modulation, the electrons are injected from the outer edge of the left separate-confinement-heterostructure (SCH) region and the holes from the outer edge of the right SCH region. The injected carriers diffuse through the SCH region and are captured into the QWs before recombining via the stimulated emission process. The transport effects can be modeled by taking into account the carrier density in the SCH region, the carrier density in the well region, and the photon density separately. Coupling of the carrier density in the barrier states above the QWs to the carrier density in the QWs is modeled by two terms representing carrier capture and escape into or from the wells, respectively. In this case, three rate equations are needed. The source term enters through the injection current in electrical modulation. The model considers carrier injection from the outer edges of the SCH region, diffusion across the SCH region, and the subsequent capture and emission of carriers by the OW.

Optical Injection For optical injection using an external pump laser, the pump photon density acts as the source term. Because the optical energy of the pump laser determines whether the photons are absorbed in the well or in the barriers, we choose the pump wavelength to be longer than the band-gap wavelength of the barriers and shorter than the band-edge wavelength of the wells so that absorption occurs only in the wells. Compared with electrical modulation, optical modulation with an optical energy in the absorption range of the QW directly produces photon-generated carriers inside the test laser's active region via the injection of a modulated laser beam through one of the test laser's mirror facets. Therefore, the majority of carriers transporting through the SCH region is not required for lasing action, although the coupling between SCH and QW states still exists for optical modulation. In this way, optical modulation removes the severe low-frequency roll-off due to the transport and parasitic effects and helps to clarify the intrinsic response.

The rate equations for both electrical and optical injections are written as

$$\frac{dN_{b}(t)}{dt} = \eta_{i} \frac{I(t)}{qV_{b}} - \frac{N_{b}(t)}{\tau_{b}} - \frac{N_{b}(t)}{\tau_{bw}} + \frac{N_{w}(t)V_{w}}{\tau_{wb}V_{b}} \tag{12.3.1}$$

$$\frac{dN_{w}(t)}{dt} = \frac{N_{b}(t)V_{b}}{\tau_{bw}V_{w}} - \frac{N_{w}(t)}{\tau_{w}} - \frac{N_{w}(t)}{\tau_{wb}} - v_{g} \frac{g(N_{w})}{1 + \varepsilon S} + v_{g} \alpha_{p} S_{p}(t) \tag{12.3.2}$$

$$\frac{dS(t)}{dt} = \Gamma v_{g} \frac{g(N_{w})}{1 + \varepsilon S} + \frac{S(t)}{\tau_{p}} \tag{12.3.3}$$

where q is the electron unit charge,  $g(N_{\rm w})$  is the optical gain at the carrier concentration  $N_{\rm w}$  in the bound states of the wells,  $N_{\rm b}$  is the carrier density in the barrier (continuum) states including the SCH and active layers, S is the photon density of

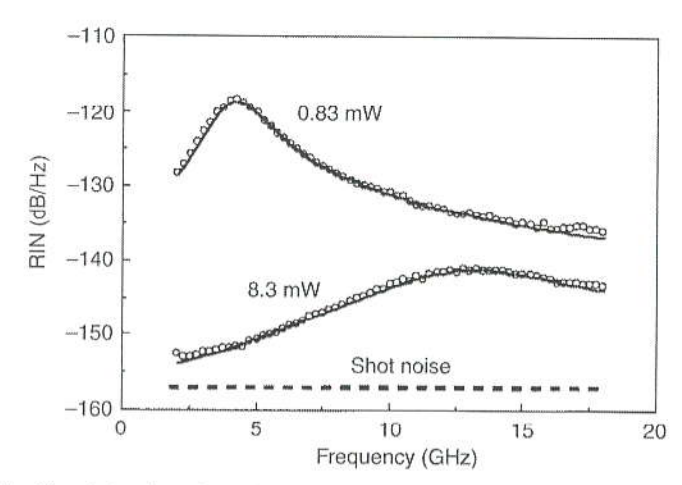


Figure 12.12 The relative intensity noise (RIN) spectrum as two bias currents above threshold. The symbols are experimental data and the solid curves are the theoretical fits. The shot noise background is also shown as the dashed line. (Reprinted with permission from [86] © 1992 IEEE.)

of the frequency. The RIN spectrum is thus given by

$$\frac{\text{RIN}}{\Delta f} = \frac{2S_{\delta p}(\omega)}{P_0^2}.$$
(12.5.12)

Further derivations for the spectral density using (12.5.6) and (12.5.7) lead to [83, 85]

$$S_{\delta p}(\omega) = \hbar \omega P_0 \left[ (a_1 + a_2 \omega^2) \frac{|H(\omega)|^2}{\omega_r^4} + 1 \right]$$
 (12.5.13)

$$\frac{\text{RIN}}{\Delta f} = \frac{2\hbar\omega}{P_0} \left[ (a_1 + a_2\omega^2) \frac{|H(\omega)|^2}{\omega_r^4} + 1 \right].$$
 (12.5.14)

Typically, the last term (one) in the square bracket of (12.5.14) is much smaller than the leading two terms, and is thus negligible [85]. The expression requires essentially four parameters:  $a_1$ ,  $a_2$ ,  $\omega_r$ , and  $\gamma$ , which can be extracted by fitting the experimental RIN spectrum at various bias current above threshold. Figure 12.12 shows an example of the RIN spectrum at two bias currents (symbols: experimental data; solid curves: theory) [86]. The extracted relaxation frequency from the peak of the RIN spectrum shows a linear dependence on the square root of the optical power output. The damping factor  $\gamma$  also shows a linear dependence on the squared relation frequency with the slope determined by the K factor. The RIN characteristics of a semiconductor laser under the injection locking condition shows a reduction in the RIN noise floor as well as an increase of the relaxation frequency controllable by the injection laser power and detuning [87].

-relaxation

### 13.3.2 Directional Coupler Modulator

For an incident optical beam into waveguide a in a directional coupler modulator, the output power is

$$P_b = |b(\ell)|^2 = \frac{|K|^2}{\Psi^2} \sin^2(\Psi \ell)$$
 (13.3.7a)

$$\Psi = \left[ \left( \frac{\Delta \beta}{2} \right)^2 + K^2 \right]^{1/2} \tag{13.3.7b}$$

and

$$P_a = P_{\rm in} - P_b = 1 - |b(\ell)|^2 \tag{13.3.8}$$

where the input power is assumed to be 1. Because  $\Delta\beta\simeq\beta_a-\beta_b=kn_o^3r_{63}V/d$ , we plot the output power  $P_a$  versus  $\Delta\beta\ell$ . Suppose we design the modulator with a length  $\ell$  such that  $P_a=0$ , and  $P_b=1$ , at  $\Delta\beta=0$  (i.e.,  $K\ell=\pi/2$ ). In order to switch to  $P_a=1$ , and  $P_b=0$ , we require at least  $\Delta\beta\ell=\sqrt{3}\pi$ , assuming the field-induced change in the refractive index affects the coupling coefficient negligibly. (Otherwise, we can calculate the field-dependent K and still use the expressions for  $P_a$  and  $P_b$  in (13.3.7) and (13.3.8) to find the output powers.) To switch from a cross state to a parallel state, the applied voltage has to be large enough such that  $\Delta\beta\ell=\sqrt{3}\pi$  is satisfied. A plot of  $P_a$  versus  $\Delta\beta\ell$  for  $K\ell=\pi/2$  is shown as the thick solid curve in Fig. 13.10. We also plot  $P_a$  versus  $\Delta\beta\ell$  for  $K\ell=\pi$ , and  $K\ell=3\pi/2$ . We see that complete switching from the  $\otimes$  (cross) state to the  $\ominus$  (parallel) state is possible (for  $K\ell=\pi/2$  or  $3\pi/2$ ). For  $K\ell=\pi$ , where we start with the parallel state at  $\Delta\beta\ell=0$ , it is impossible to switch to the  $\otimes$  state simply by changing  $\Delta\beta\ell$  alone. This fact can also be checked with the switching diagram in Fig. 8.11.

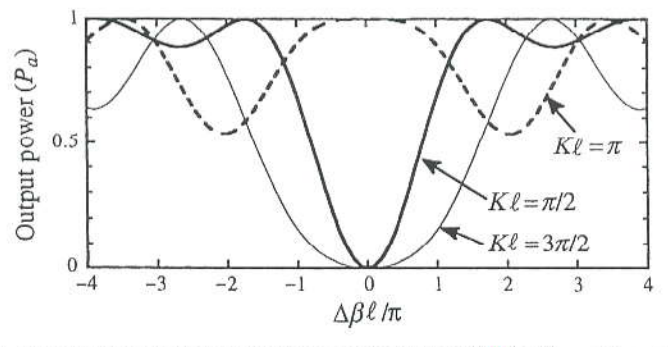


Figure 13.10 The output power from waveguide a as a function of  $\Delta\beta L$  for  $K\ell = \pi/2$ ,  $\pi$ , and  $3\pi/2$  for a directional coupler modulator.

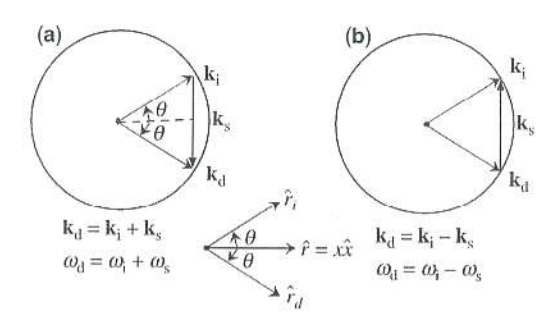


Figure 13.14 The diagrams for the diffraction of light by sound: (a)  $k_d = k_i + k_s$ ,  $\omega_d = \omega_i + \omega_s$ , and (b)  $\mathbf{k}_{\mathrm{d}} = \mathbf{k}_{\mathrm{i}} - \mathbf{k}_{\mathrm{s}}, \ \omega_{\mathrm{d}} = \omega_{\mathrm{i}} - \omega_{\mathrm{s}}.$ 

reduced

Similarly, (13.5.13) corresponds to the emission of a phonon from the incident photon. Here h is the Planck constant. Also noting that  $k_i = \frac{\omega_i}{c} n$ , and  $k_d = \frac{\omega_d}{c} n$ , we find from (13.5.6) and (13.5.10)

$$i\mathbf{k}_{\mathrm{i}} \cdot \nabla E_{\mathrm{i}} = ik_{\mathrm{i}} \frac{\partial E_{\mathrm{i}}}{\partial r_{\mathrm{i}}} = -\frac{\omega_{\mathrm{i}}^{2} n}{2c^{2}} \Delta n E_{\mathrm{d}}(r).$$

Because  $\mathbf{r}_i$  is along the direction of  $\mathbf{k}_i,$  and  $\mathbf{r}_d$  is along the direction of  $\mathbf{k}_d,$  we take ralong the x direction, and

$$r_i \cos \theta = x,$$
  $r_d \cos \theta = x.$  (13.5.14)

We obtain

$$\frac{dE_{i}}{dx} = iK_{id}E_{d} \qquad K_{id} = \frac{\omega_{i}\Delta n}{2c\cos\theta}$$
 (13.5.15a)

$$\frac{dE_{i}}{dx} = iK_{id}E_{d} \qquad K_{id} = \frac{\omega_{i}\Delta n}{2c\cos\theta}$$

$$\frac{dE_{d}}{dx} = iK_{di}E_{i} \qquad K_{di} = \frac{\omega_{d}\Delta n}{2c\cos\theta}.$$
(13.5.15a)

Because  $\omega_s \ll \omega_i$ ,  $\omega_d$  we have  $\omega_d \sim \omega_i \equiv \omega$  and  $K_{di} \simeq K_{id} \equiv K$ 

$$K = \frac{\omega \Delta n}{2c \cos \theta}.$$
 (13.5.16)

The solutions for the coupled-mode equation given the initial conditions  $E_i(0)$  and  $E_{\rm d}(0)$  are

$$E_{i}(x) = E_{i}(0)\cos Kx + iE_{d}(0)\sin Kx$$
  

$$E_{d}(x) = E_{d}(0)\cos Kx + iE_{i}(0)\sin Kx.$$
(13.5.17)

If initially,  $E_d(0) = 0$ , the field amplitudes are

$$E_{i}(x) = E_{i}(0)\cos Kx$$
  $E_{d}(x) = iE_{i}(0)\sin Kx.$  (13.5.18)

REFERENCES 667

 S. Adachi, Physical Properties of III-V Semiconductor Compounds, Wiley, New York, 1992.

- K. H. Hellwege, Ed., Landolt-Börnstein Numerical Data and Functional Relationships in Science and Technology, New Series, Group III 17a, Springer-Verlag, Berlin, 1982; Groups III-V 22a, Springer-Verlag, Berlin, 1986.
- K. Tada and N. Suzuki, "Linear electrooptical properties of InP," *Jpn. J. Appl. Phys.* 19, 2295–2296 (1980); and N. Suzuki and K. Tada, "Electrooptic properties and Raman scattering in InP," *Jpn. J. Appl. Phys.* 23, 291–295 (1984).
- S. Adachi and K. Oe, "Linear electro-optic effects in zincblende-type semiconductors: key properties of InGaAsP relevant to device design," J. Appl. Phys. 56, 74–80 (1984); and "Quadratic electrooptic (Kerr) effects in zincblende-type semiconductors: Key properties of InGaAsP relevant to device design," J. Appl. Phys. 56, 1499–1504 (1984).
- S. Adachi, Properties of Indium Phosphide, INSPEC, The Institute of Electrical Engineers, London and New York, 1991.
- A. K. Ghatak and K. Thyagarajan, Optical Electronics, Cambridge University Press, Cambridge, UK, 1989.
- M. Abramowitz and I. A. Stegun, Eds., Handbook of Mathematical Functions with Formulas, Graphs, and Mathematical Tables, Chapter 9, Dover, New York, 1972.
- S. Thaniyavarn, "Optical modulation: electrooptical Devices," Chapter 4 in K. Chang, Ed., Handbook of Microwave and Optical Components, vol. 4 of Fiber and Electro-Optical Components, Wiley, New York, 1991.
- H. Nishihara, M. Haruna, and T. Suhara, Optical Integrated Circuits, McGraw-Hill, New York, 1989.
- 13. T. Tamir, Ed., Guided-Wave Optoelectronics, 2nd ed., Springer-Verlag, Berlin, 1990.
- R. C. Alferness, "Guided-wave devices for optical communication," *IEEE J. Quantum Electron.* QE-17, 946–959 (1981).
- O. G. Ramer, "Integrated optic electrooptic modulator electrode analysis," *IEEE J. Quantum Electron.* QE-18, 386–392 (1982).
- D. Marcuse, "Optimal electrode design for integrated optics modulators," IEEE J. Quantum Electron. QE-18, 393–398 (1982).
- H. Kogelnik and R. V. Schmidt, "Switched directional couplers with alternating Δβ," IEEE J. Quantum Electron. QE-12, 396–401 (1976).
- K. Noguchi, O. Mitomi, H. Miyazawa, and S. Seki, "A broadband Ti:LiNbO<sub>3</sub> optical modulator with a ridge structure," *J. Lightwave Technol.* 13, 1164–1168 (1995).
- O. Mitomi, K. Noguchi, and H. Miyazawa, "Design of ultra-broadband LiNbO<sub>3</sub> optical modulators with ridge structure," *IEEE Trans. Microwave The. Techn.* 41, 2203–2207 (1995).
- O. Mitomi, K. Noguchi, and H. Miyazawa, "Broadband and low driving-voltage LiNbO<sub>3</sub> optical modulators," *IEE Proc. Optoelectron.* 145, 360–364 (1998).
- E. L. Wooten, K. M. Kissa, A. Yi-Yan, E. J. Murphy, D. A. Lafaw, P. F. Hallemeier, D. Maack, D. V. Attanasio, D. J. Fritz, G. J. McBrien, and D. E. Bossi, "A review of lithium niobate modulators for fiber-opticcommunications systems," *IEEE J. Sel. Top. Quantum Electron.* 6, 69–82 (2000).

43 (Bold)

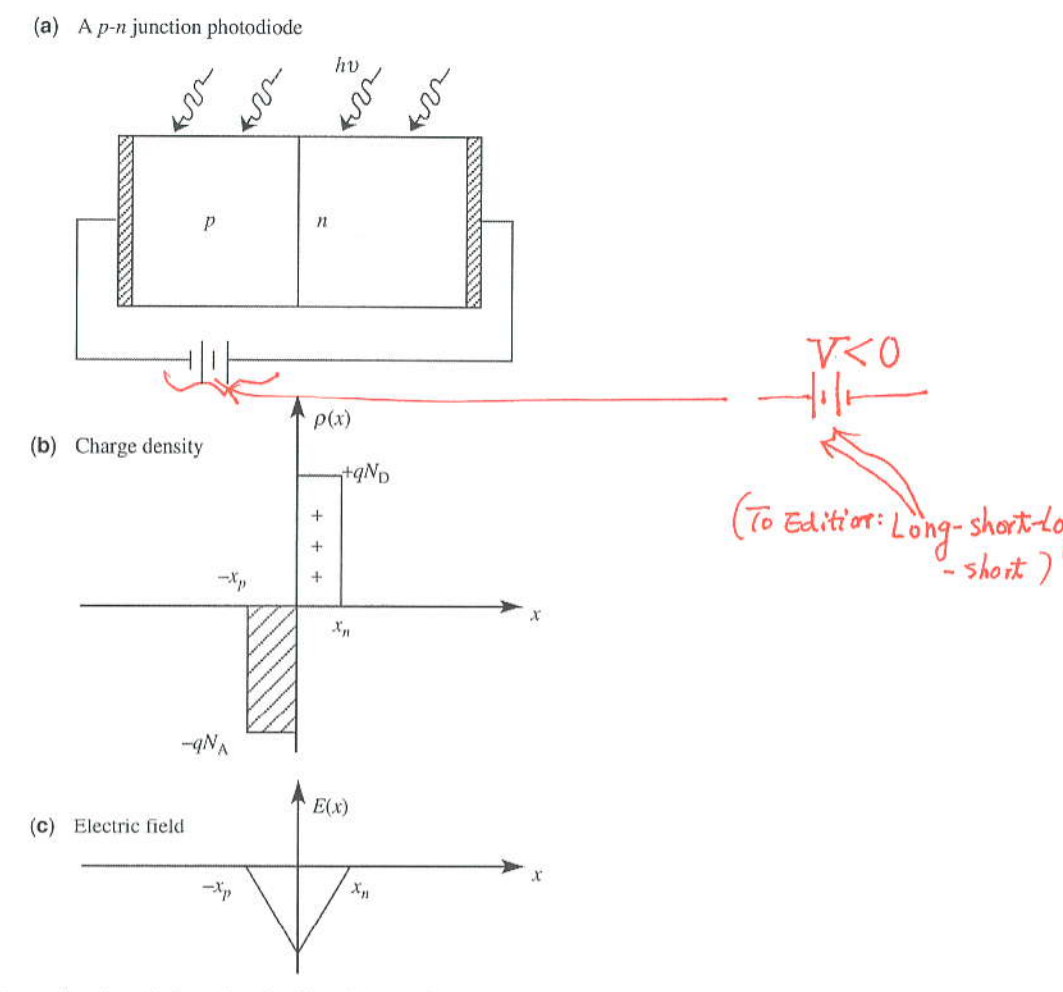


Figure 15.4 (a) A p-n junction diode under the illumination of a uniform light. (b) The charge distribution p(x) under depletion approximation. (c) The electric field E(x) obtained from Gauss's law.

Because  $p_{n0}$  is independent of x and t, we have at steady state if  $G(x, t) = G_0$  is independent of x and t,

$$D_p \frac{\partial^2}{\partial x^2} \delta p_n - \frac{\delta p_n}{\tau_p} = -G_0. \tag{15.2.3}$$

The above equation can be solved by summing the homogeneous and particular solutions

$$\delta p_n(x) = c_1 e^{-(x-x_n)/L_p} + c_2 e^{(x-x_n)/L_p} + G_0 \tau_p$$
 (15.2.4)

where  $L_p = \sqrt{D_p \tau_p}$  is the diffusion length for holes. The particular solution is due to the optical generation. If the *n*-region is very long, we can set  $c_2 = 0$ ; otherwise,

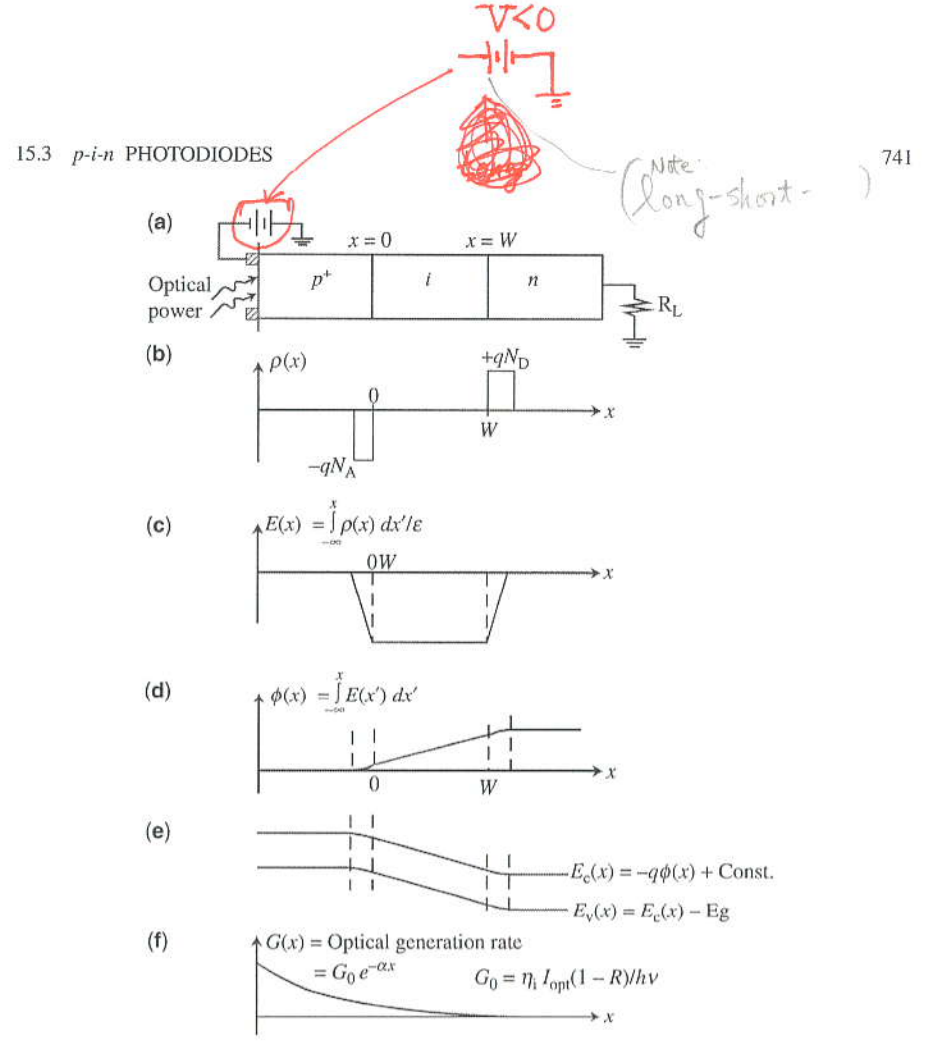


Figure 15.6 (a) A p-i-n photodiode under optical illumination from the p<sup>+</sup>-side, (b) the charge density  $\rho(x)$  under depletion approximation, (c) the static electric field profile E(x), (d) the electrostatic potential  $\varphi(x)$ , (e) the conduction and valence band edge profiles, and (f) the optical generation rate G(x).

At steady state, the total photocurrent density consists of both a drift and a diffusion component

$$J = J_{dr} + J_{diff}. \tag{15.3.3}$$

Considering the  $p^+$ -region to be of negligible thickness, we look at the contribution in the intrinsic region 0 < x < W

$$J_{\rm dr} = -q \int_{0}^{W} G(x)dx = -qS_0(1 - e^{-\alpha W}) = -q\eta\Phi(\lambda)$$
 (15.3.4a)

$$\eta = \eta_1 (1 - R)(1 - e^{-\alpha W}) \tag{15.3.4b}$$

where the minus sign of the drift current density accounts for the fact that the drift current flows in the -x direction, and  $\eta$  is the quantum efficiency including the effects of surface reflectivity R and finite thickness of the absorption layer W.

proportional to the optical intensity profile in the device

$$G(x, \lambda) = G_0 e^{-\alpha(\lambda)x}$$

$$G_0 = \eta_i [1 - R(\lambda)] \Phi(\lambda) \alpha(\lambda)$$
(15.6.8)

d(2) -

where  $\lambda$  is the absorption spectrum,  $\Phi(\lambda) = I_{\rm opt}/\hbar\omega$  is the optical flux density for an incident optical power intensity  $I_{\rm opt}$  (W/cm<sup>2</sup>), and  $\eta_i$  is the intrinsic quantum efficiency to account for the average number (100% maximum) of electron-hole pairs generated per incident photon. Figure 15.21d shows the energy band diagram and the quasi-Fermi levels for a small forward bias voltage (defined as positive for the p-electrode). To obtain the I-V curve of a p-n junction solar cell, the key steps are essentially the same as those for photodiodes.

- Find the minority carrier density in the quasi-neutral region of the n and p region in the presence of optical illumination with an incident photon flux (optical intensity) at a given wavelength λ for the given generation rate G(x, λ). The major equations are the diffusion equations in the presence of carrier generation. The carrier densities or current densities have to satisfy the required boundary conditions.
- 2. Calculate the minority current density at the edge of the depletion region, that is,  $J_p(\lambda)$  at  $x = x_j$  (=  $W_n x_n$ ) on the *n*-side, and  $J_n(\lambda)$  at  $x = x_j + x_w$  the *p*-side, where  $x_w$  is the depletion width.
- 3. Calculate the contribution due to the drift current density due to optical generation in the depletion region  $J_{\rm dr}(\lambda)$

$$J_{dr}(\lambda) = q \int_{x_j}^{x_j + x_w} G_0 e^{-\alpha x} dx$$
  
=  $q \eta_i [1 - R(\lambda)] \Phi(\lambda) e^{-\alpha x_j} (1 - e^{-\alpha x_w}).$  (15.6.9)

4. The total current density for an incident photon flux at a given wavelength is

$$J(\lambda) = J_n(\lambda) + J_n(\lambda) + J_{dr}(\lambda). \tag{15.6.10}$$

5. The spectral response is defined as

$$S_{\rm R}(\lambda) = \frac{J(\lambda)}{q[1 - R(\lambda)]\Phi(\lambda)}.$$
 (15.6.11)

6. The total photocurrent is obtained by integrating the product of the transmitted photon flux into the solar cell and the spectral response to the maximum

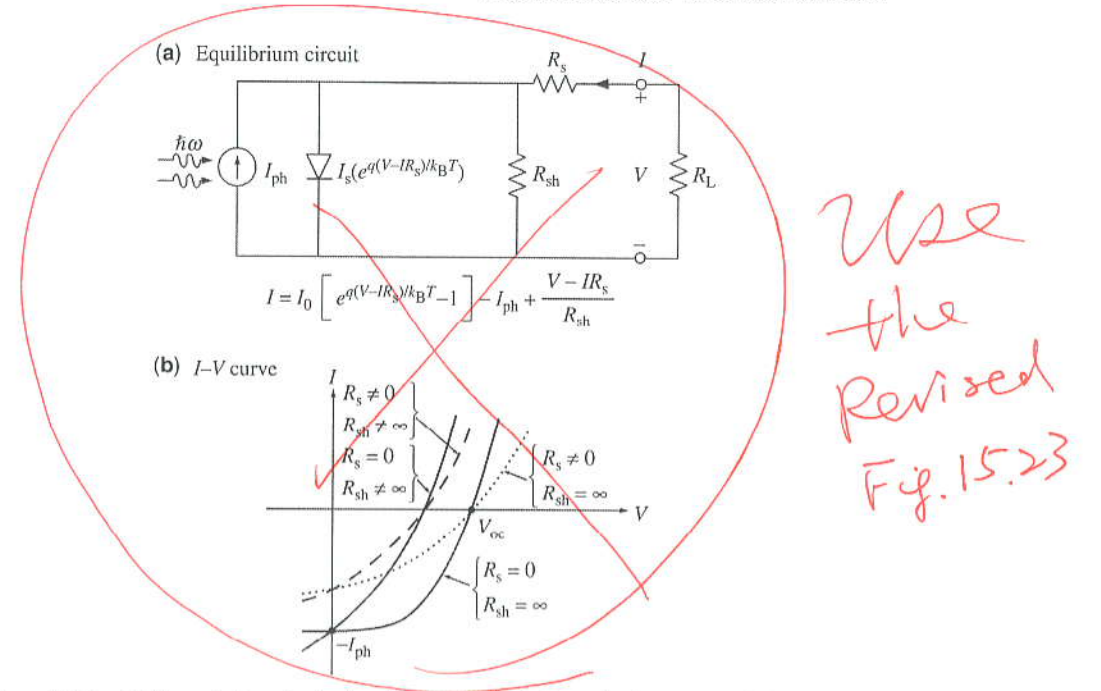


Figure 15.23 (a) The equivalent circuit of a solar cell. (b) The I-V curve in the presence of shunt  $(R_{\rm sh})$  and series  $(R_{\rm s})$  resistances. In an ideal solar cell, the shunt resistance is infinity and the series resistance is zero.

conversion efficiency is reduced, as shown in Fig. 15.23b

$$I = I_0 \left[ e^{q(V - IR_s)/\gamma k_B T} - 1 \right] - I_{\text{ph}} + \frac{V - IR_s}{R_{\text{sh}}}.$$
 (15.6.25)

### 15.6.3 Quantum-Well and Multijunction Solar Cells

**Quantum-Well Solar Cells** By placing multiple quantum wells [111–121] in the intrinsic region of a *p-i-n* structure, it is possible to realize solar cells with improved quantum efficiency, Fig. 15.24. It is important to maintain the built-in field across

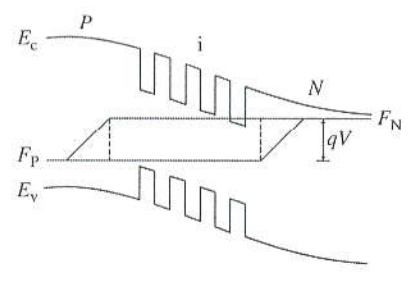
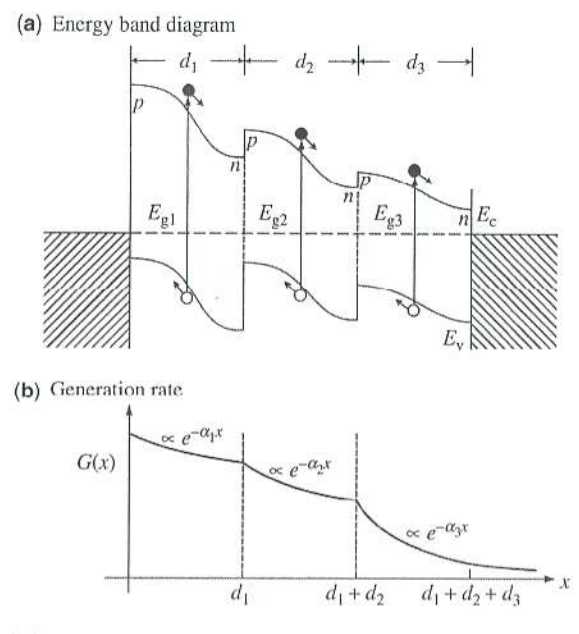
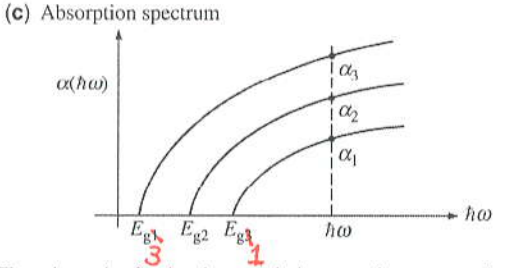


Figure 15.24 A multiple quantum-well (MQW) solar cell in a *P-I-N* structure. The intrinsic region contains many quantum wells for enhanced absorption.





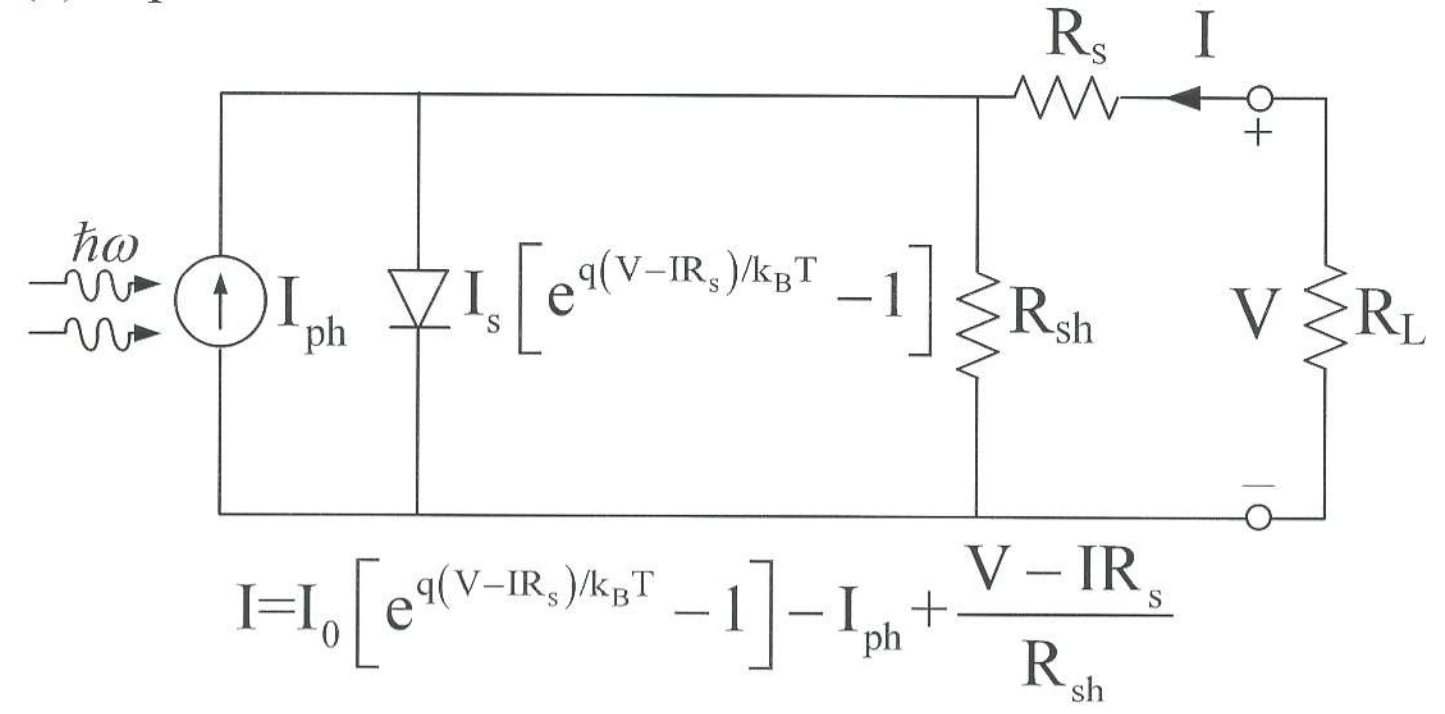
**Figure 15.26** (a) The schematics for the electron—hole generation rate as a function of optical depth into the multijunction solar cell from the top wide band gap into the bottom narrow band gap region. (b) The generation rate of electron—hole pairs is proportional to the optical intensity, which decays as a function of position *x*. (c) The absorption spectra of the three band gaps.

(use Revised Fig. 15.26)

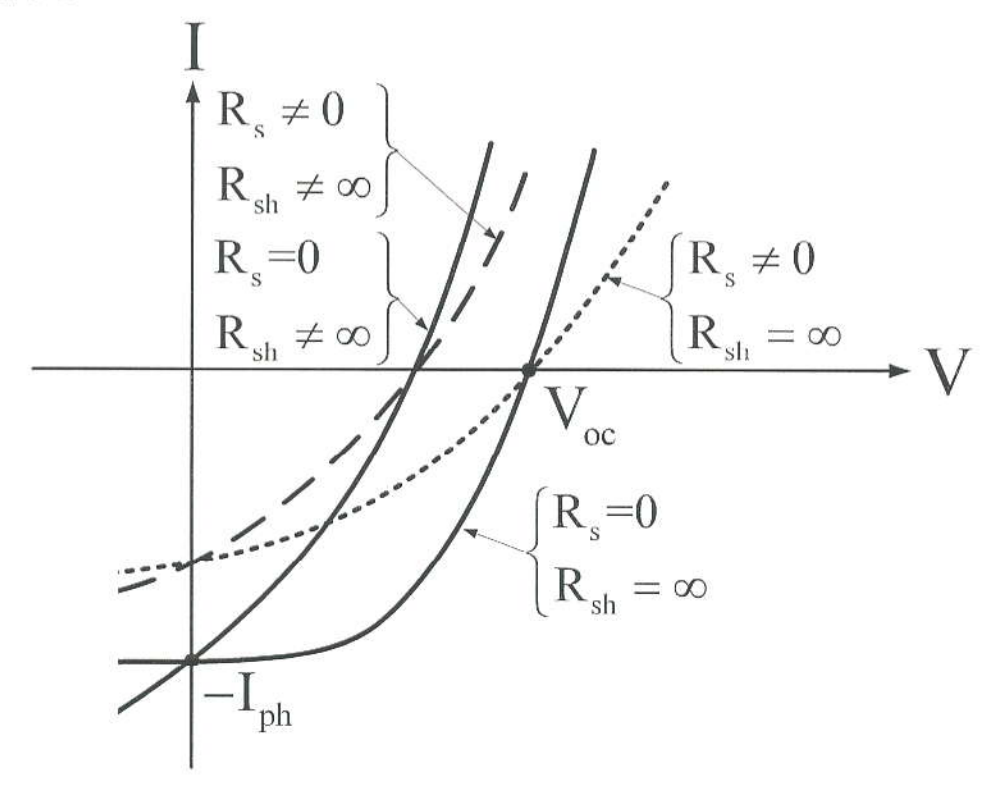
can be lattice-matched to substrates such as Si, Ge, and GaAs, with band gaps that are complementary to those of other III-V compound semiconductors. The absorption spectra of some of these materials have been shown in Chapter 2, Fig. 2.4. Poor minority carrier transport in III-N-V materials is a critical research issue.

Figure 15.26a shows the schematic for the electron-hole generation rate as a function of optical depth into the multijunction solar cell from the top wide band gap into the bottom narrow band gap region. Figure 15.26b shows the generation rate per unit volume of the electron-hole pairs, which is proportional to the optical intensity that decays into the solar cell depth. The absorption spectra of all three band gaps are illustrated in Fig. 15.26c. The absorption of the solar radiation spectrum by different band gap layers allows for the conversion of more photons into electron and hole pairs. Carrier transport and collection become important

(a) Equilibrium Circuit

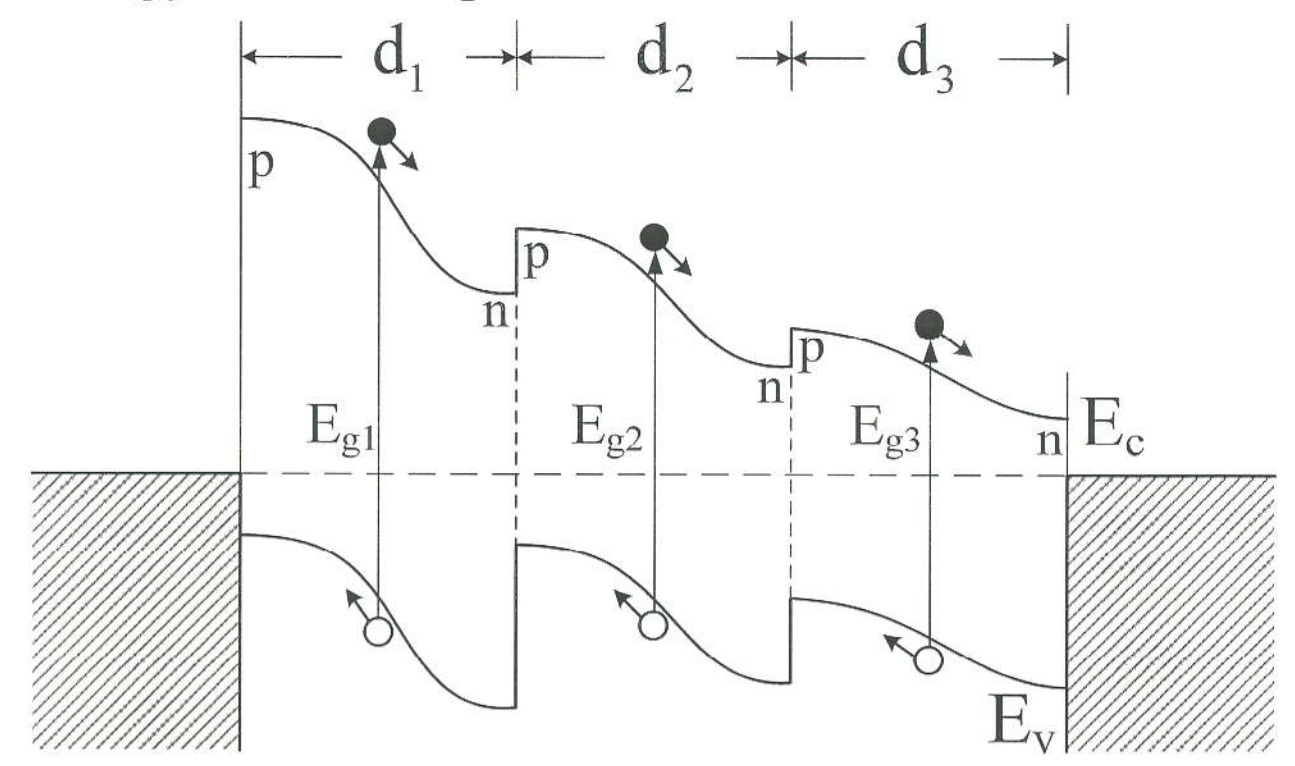


(b) I-V Curve

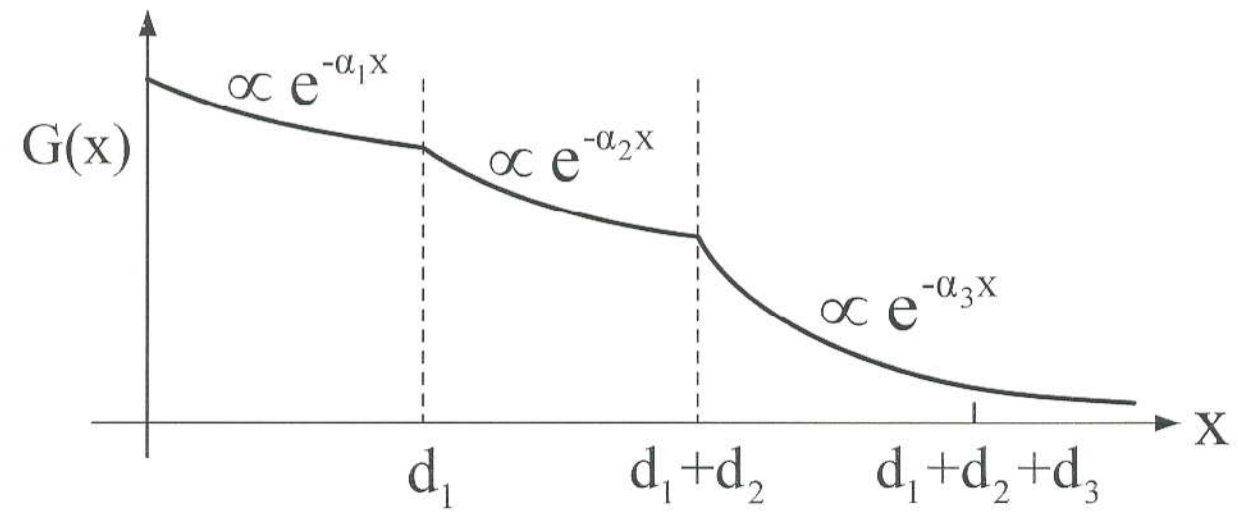


New (Revised) Figure 15.23

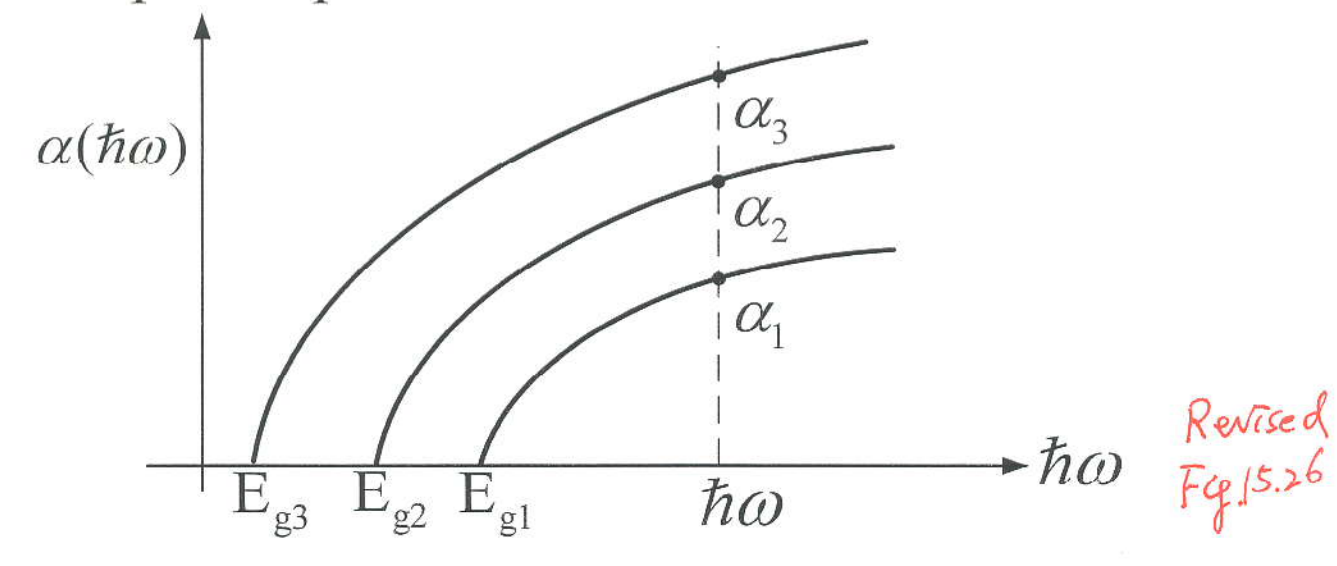
### (a) Energy Band Diagram



## (b) Generation Rate



### (c) Absorption Spectrum



# 1

## These two pages are missing in the First Print. This 4 the next page should be printed in the inside of the Bottom Cover.

Physical Constants	Symbol	Numerical Values
Speed of light in free space	c	$= 2.9979 \times 10^8 \mathrm{m/s}$
Permittivity in free space	$arepsilon_0$	$= 8.8542 \times 10^{-12}  \text{F/m}$
		$\left(\simeq \frac{1}{36\pi} \times 10^{-9} \mathrm{F/m}\right)$
Permeability in free space	$\mu_0$	$=4\pi \times 10^{-7} \text{ H/m}$
Boltzmann constant	$k_{ m B}$	$=1.3807 \times 10^{-23} \text{ J/K}$
Elementary charge	q or $e$	$=1.60219 \times 10^{-19} \text{ C}$
Free electron mass	$m_0$	$=9.1095 \times 10^{-31} \text{ kg}$
Planck constant	h	$= 6.6262 \times 10^{-34} \text{ Js}$
Reduced Planck constant	. h	$\zeta = 1.05459 \times 10^{-34}  \text{Js}$
	$h = \frac{1}{2\pi}$	$\begin{cases} = 1.05459 \times 10^{-34} \text{ Js} \\ = 6.5822 \times 10^{-16} \text{ eVs} \end{cases}$
Angstrom unit	1 Å	$=10^{-10}\text{m}=10^{-8}\text{cm}=10^{-4}\mu\text{m}$
Bohr radius	$a_0 = \frac{4\pi\varepsilon_0 \hbar^2}{e^2 m_0}$	= 0.529177 Å
Ryberg energy	$R_{\rm y} = \frac{m_0 e^4}{2(4\pi\varepsilon_0)^2 \hbar^2}$	$=\frac{\hbar^2}{2m_0} \left(\frac{1}{a_0}\right)^2 = 13.6058 \text{eV}$
Energy unit (electron-volt)		$= 1.60219 \times 10^{-19} \mathrm{J}$
Thermal energy at 300 K	$k_{\mathrm{B}}T$	$= 25.853 \mathrm{meV}$

Useful Formulas and Physical Quantities		
Photon energy	$\hbar\omega = h\frac{c}{\lambda} = \frac{1.2398}{\lambda} \text{ eV}, \text{ where } \lambda \text{ is in } (\mu\text{m})$	
Rydberg of an exciton	$R_{\rm y} = \frac{m_{\rm r}e^4}{2(4\pi\varepsilon_{\rm s})^2\hbar^2} = \frac{(m_{\rm r}/m_0)}{(\varepsilon_{\rm s}/\varepsilon_0)^2} \times 13.6058\mathrm{eV}$	
Bohr radius of an exciton	$a_0 = \frac{4\pi\varepsilon_{\rm s}\hbar^2}{e^2m_{\rm r}} = \frac{\varepsilon_{\rm s}/\varepsilon_0}{m_{\rm r}/m_0} \times 0.529177 \text{ Å}$	
Quantized subband energy in a quantum well (infinite barrier model)	$E = \frac{\hbar^2}{2m^*} \left(\frac{n\pi}{L}\right)^2$ = $\frac{n^2}{(m^*/m_0)} \frac{1}{L^2} \times 37.6033 \text{ eV } (L \text{ is in Å})$	
Conduction band density parameter	$N_{\rm e} = 2 \left( \frac{m_{\rm e}^* k_{\rm B} T}{2 \pi \hbar^2} \right)^{3/2} = 2.51 \times 10^{19} \left( \frac{m_{\rm e}^*}{m_0} \frac{T}{300} \right)^{3/2} {\rm cm}^{-3}$	

## Inside the Bottom Cover

### (1) Maxwell's Equations

$$\nabla \times \mathbf{E} = -\frac{\partial}{\partial t} \mathbf{B}$$

$$\nabla \times \mathbf{H} = \mathbf{J} + \frac{\partial \mathbf{D}}{\partial t}$$

$$\nabla \cdot \mathbf{D} = \rho$$

$$\nabla \cdot \mathbf{B} = 0$$

(3) Density-of-States, 
$$\rho_c$$
 (E)

3D 
$$\frac{1}{2\pi^2} \left(\frac{2m_{\rm c}^*}{\hbar^2}\right)^{3/2} \sqrt{E}$$

2D 
$$\frac{m_{\rm c}^*}{\pi h^2 L_z} \sum_{n} H(E - E_n)$$

1D 
$$\frac{1}{\pi L_x L_y} \sqrt{\frac{2 m_c^*}{h^2}} \sum_{n_c,n_c} \frac{1}{\sqrt{E - E_{n_c} - E_{n_c}}}$$

### Continuity Equation

$$\nabla \boldsymbol{\cdot} \, \mathbf{J} + \frac{\partial}{\partial t} \boldsymbol{\rho} = 0$$

### (2) Semiconductor Electronics Equations

$$\nabla \cdot (\varepsilon \nabla \phi) = -q(p-n+N_{\mathrm{D}}^{+}-N_{\mathrm{A}}^{-})$$

$$\frac{\partial n}{\partial t} = G_n - R_n + \frac{1}{q} \nabla \cdot \mathbf{J}_n$$

$$\frac{\partial p}{\partial t} = G_p - R_p - \frac{1}{q} \nabla \cdot \mathbf{J}_p$$

$$\mathbf{J}_n = q\mu_n n\mathbf{E} + qD_n \nabla n$$

$$\mathbf{J}_p = q\mu_p p \mathbf{E} - q D_p \nabla p$$

$$\mathbf{E} = -\nabla \phi$$

### (4) Fermi Distribution

Electron in conduction band

$$f_{c}(E) = \frac{1}{1 + e^{(E - F_{c})/k_{B}T}}$$

Electron occupation probability in valence band

$$f_{v}(E) = \frac{1}{1 + e^{(E - F_{v})/k_{\rm B}T}}$$

Hole in valence band

$$f_{\rm h}(E) = 1 - f_{\rm v}(E) = \frac{1}{1 + e^{(F_{\rm v} - E)/k_{\rm B}T}}$$